ACS APPLIED ENERGY MATERIALS

www.acsaem.org Article

Asymmetrically Substituted Phthalocyanines as Dopant-Free Hole Selective Layers for Reliability in Perovskite Solar Cells

Peng Huang,[⊥] Adrián Hernández,[⊥] Samrana Kazim, Jorge Follana-Berná, Javier Ortiz, Luis Lezama, Ángela Sastre-Santos,* and Shahzada Ahmad*

Cite This: *ACS Appl. Energy Mater.* 2021, 4, 10124−10135 Read Online

ACCESS | Metrics & More | Article Recommendations | Supporting Information

ABSTRACT: Dopant-free metal phthalocyanines are viable alternatives to the classical 2,2′,7,7′-tetrakis-(*N*,*N*-di-*p*-methoxyphenylamine)-9,9′-spirobifluorene (Spiro-OMeTAD) in perovskite solar cells (PSCs), due to their appealing optoelectrical properties and chemical stability. However, low carrier concentration, transportability, and narrow band gap limit their application. Here, we designed and investigated six innovative asymmetrically substituted metal phthalocyanines (MPcs, M = Zn or Cu), and established the correlation among the electronic structure, charge carrier transfer parameter, and core metal/substitutions in MPcs by transient absorption spectroscopy and electron paramagnetic resonance. We probed the charge transport properties of ZnPcs including their carrier lifetime, diffusion coefficient, and diffusion length by transient absorption spectroscopy. We noted that ZnPcAE presents a longer diffusion length (1.94 nm) than the control ZnPcTB4 (0.80 nm), which is advantageous for reducing charge recombination and gives a higher power conversion efficiency in the fabricated PSCs. Importantly, the devices with MPcs yielded improved stability under multistress conditions. Our work provides a molecular guideline for designing MPcs and their application as dopant-free hole-transporting materials for perovskite solar cell fabrication.

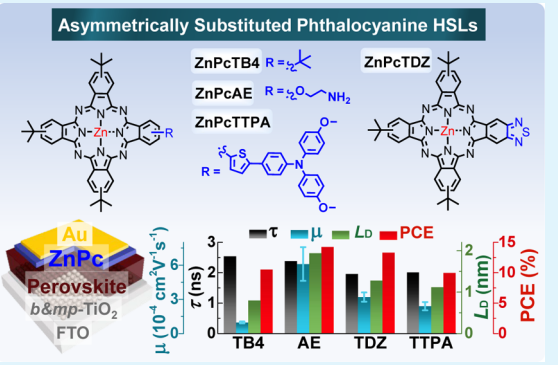

KEYWORDS: *perovskite solar cells, metal phthalocyanine, hole-transporting materials, improved stability, electron paramagnetic resonance, transient absorption*

1. INTRODUCTION

Hybrid organic−inorganic perovskite solar cells (PSCs) have attracted significant interest, as their certificated power conversion efficiency (PCE) swiftly soared from 10 to 25.5% in less than a decade.[1−3] This rapid advancement in the figure of merit was due to the unparalleled characteristics of hybrid organic−inorganic perovskites: tunable panchromatic light absorption, long carrier diffusion lengths for electrons/holes, and low-temperature solution-processability.[4−6] To accelerate the commercial viability of perovskite-based devices, investigations on the stability of perovskites and devices are receiving substantial attention. Designing innovative electron/hole-transporting materials (ETM/HTM)[7,8] and placement of a buffer layer at the different interfaces[9] allowed us to optimize the photovoltaic (PV) performance and device stability.[10,11]

In typical (n-i-p) PSCs, HTM-coated perovskite layers play crucial roles in separating and extracting photogenerated holes, suppressing interface charge recombination, to achieve high PCE. The choice of HTMs can extend the durability of the devices by isolating the perovskite active layer from oxygen and moisture, and passivating the surface defect. Although 2,2′,7,7′-tetrakis-(*N*,*N*-di-*p*-methoxyphenylamine)-9,9′-spirobifluorene (Spiro-OMeTAD) is the most employed HTM in n-i-p type PSCs, the pristine Spiro-OMeTAD possesses poor electrical properties, UV instability, and is cost-ineffective.[12,13] Further the use of hygroscopic p-type dopants and additives such as lithium bis(trifluoromethanesulfonyl)imide (Li-TFSI) and 4-*tert*-butylpyridine (*t*-BP) or a metal complex is a prerequisite to improve electrical properties, which diffuses into perovskite layers and accelerates degradation under real operating conditions.[12,13] Alternatively, developing dopant-free HTMs that can yield high PV performance and stability is paramount research.

Recently, dopant-free HTMs based on small molecules, macrocycle molecules, and conjugated polymers have been designed and their performance was reported.[14] Phthalocyanines (Pcs) are attractive as HTMs due to their ease of synthesis, purification steps, and are thermally and photochemical stable. In most of the cases, they yield competitive

Received: July 12, 2021
Published: September 10, 2021

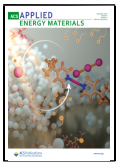

https://doi.org/10.1021/acsaem.1c02039
ACS Appl. Energy Mater. 2021, 4, 10124−10135

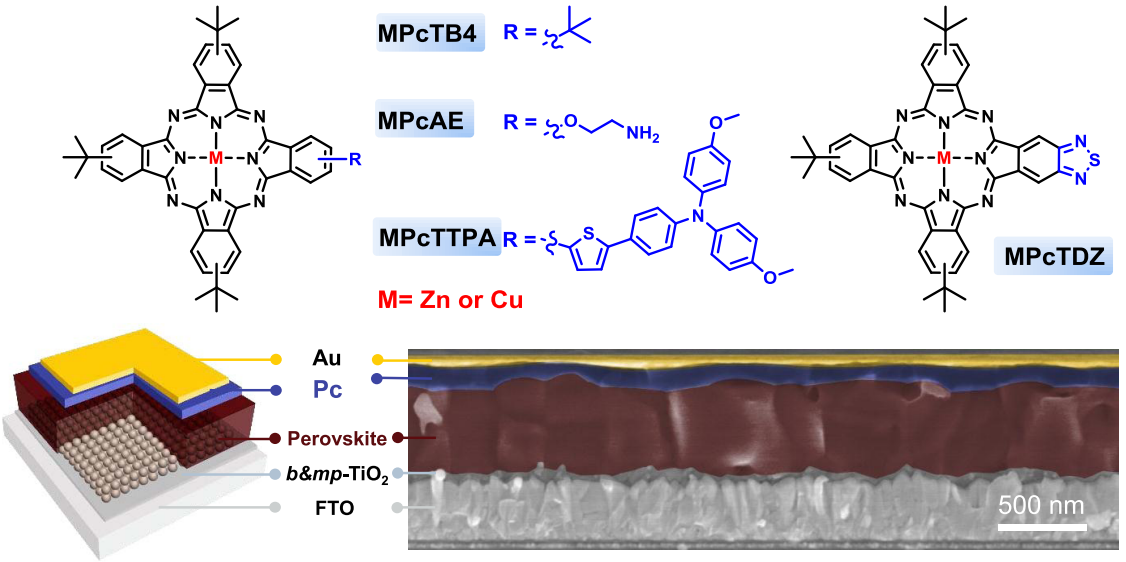

Figure 1. Molecular structures of unsymmetrical MPcs and the device architect employing MPc as an HTM, and the representative cross-sectional image of PSC with the standard architecture fluorine-doped tin oxide (FTO)/b&mp-TiO_2/perovskite/ZnPcAE/Au.

performance in PSCs,[15] being the record when using symmetrical NiPc with tetra-metoxy ethoxy substituents measured over 21% efficiency.[16]

The PV performance of PSCs employing Pcs is limited by two major factors: (i) poor conductivities of pristine Pcs. In the early stages of Pc-based HTM development, introduction of dopants (lithium salts and *t*-BP) for improvement of charge mobility were inevitable, which sacrifices the device stability.[17] Aiming at developing dopant-free Pc HTMs, various peripheral/nonperipheral substituents and different core atoms were applied into phthalocyanines.[18] Nonperipheral P-SC_6-TiOPc/peripheral-substituted NP-SC_6-TiOPc dopant-free HTMs were synthesized.[19] We have designed peripheral-substituted ZnTTPc with tetra-thienyl-methoxytriphenylamine (TTPA),[20] while a report of different tetra-methoxy−ethoxy-based Pcs with diverse core atoms (H_2, Zn, Cu, Ni, and Co) also appears.[16]

(ii) Interface recombination triggered their narrow band gap ranging from 1.4 to 2.1 eV. The phenomena induced poor electron blocking and charge recombination at the perovskite/HTM interface. Although the introduction of substituents or the interplay of central atoms can tune the band gap of Pcs and alleviate the interface recombination, the limited opportunity of band gap tuning is not effective. Improving the carrier diffusion length (L_D) of the Pcs, which was determined by the exciton or carrier lifetime (τ_E) and diffusion coefficient (D_E), as well as the carrier mobility (μ) is an effective protocol to impede the interfacial charge recombination. In this context, heavy palladium as the core atom to replace the copper atom in Pcs with octamethyl substituents was investigated and it was noted that PdPc presented longer L_D and thus delivered a higher performance.

Until now, the correlation among electronic structures, charge carrier transfer parameters (lifetime, diffusion coefficient, and diffusion length), and the core metal and substitutions in MPcs are not well deciphered. Herein, we elaborately designed a series of peripheral substituents including 2-methoxyethan-1-amine (AE), thiadiazole (TDZ), and TTPA to induce asymmetry in terms of the symmetrical MPc with four *tert*-butyl groups (M = Zn or Cu, Figure 1). Notably, asymmetrical substituted phthalocyanines owned unique photophysical and electrochemical properties as compared to symmetrical Pcs, stems from perturbing the distribution of the 18-π-delocalized electrons over the macrocycle. We unravel that the Pcs' properties are controlled by core metal and substitutions, through transient absorption (TA) and electron paramagnetic resonance (EPR), respectively. Further, to probe the practical utility, we fabricated PSCs by employing MPcs as a dopant-free HTM (Figure 1). Arguably, the fabricated devices gave excellent stability under multistress conditions (moisture, heating, and light).

2. RESULTS AND DISCUSSION

2.1. Synthesis. Synthesis of ZnPcTB4, ZnPcTDZ, and ZnPcAE were carried out following the procedures for ZnPcTB4,[21] ZnPcTDZ,[22] and ZnPcAE.[23] First, we describe the synthesis of CuPcTB4 and CuPcTDZ (Figure S1a). Due to the difficulty in the purification of CuPcTB4 and CuPcTDZ obtained from statistical cyclotetramerization of respective phthalonitriles in the presence of $Cu(OAc)_2$, it was essential to synthesize the free-base phthalocyanines from the corresponding diiminoisoindolines. H_2PcTB4 and H_2PcTDZ, were obtained by reaction of diiminoisoindoline 1[24] and diiminoisoindoline 2 and subsequent isolation by a chromatographic column with 13 and 9% yield, respectively. Then, metallation using $Cu(OAc)_2$ allowed us to obtain CuPcTB4 and CuPcTDZ with 76 and 79% yield, respectively. Second, we prepared CuPcAEBoc (Figure S1b) by statistical cyclotetramerization of phthalonitrile 3 and phthalonitrile 4 with $CuCl_2$. After purification by column chromatography, the product was obtained with a 5% yield. We removed the 2-*tert*-butoxycarbonyl group in acidic conditions obtaining CuPcAE in 88% yield.

Third, synthesis of ZnPcTTPA (Figure S1c) was performed by statistical cyclotetramerization of 4-tert-butylphthalonitrile- and 4-thienyl-methoxytriphenylamine-phthalonitrile 5,[20] in the presence of $Zn(OAc)_2$. After purification by column chromatography, ZnPcTTPA was obtained (18% yield). The ^{1}H NMR spectra of ZnPcTTPA in THF-d_8 showed well-defined aromatic and aliphatic signals (Figure S16). The three

https://doi.org/10.1021/acsaem.1c02039
ACS Appl. Energy Mater. 2021, 4, 10124−10135

isoindole units with the *tert*-butyl groups show different signals in the aromatic zone at 9.55, 9.39, and 8.32 ppm. Instead, the isoindole with the aromatic chain shows three signals at 9.39, 8.45, and 7.95 ppm. Regarding the aromatic chain, two doublets from the thiophene (9.67 and 7.50 ppm), four doublets from the phenyl group (7.91, 7.65, 7.12, and 7.00 ppm), and a singlet from the methoxy groups (3.80 ppm) are shown. Finally, for the synthesis of CuPcTTPA (Figure S1c) a similar procedure was followed, using $CuCl_2$ instead of $Zn(OAc)_2$. Subsequently, purification was made by column chromatography, and CuPcTTPA was obtained (12% yield). Due to the paramagnetic character of copper(II), characterization by NMR experiments was not possible for any CuPcs. Nevertheless, they were characterized by Fourier transform-infrared spectroscopy (FT-IR), high-resolution-matrix-assisted laser desorption ionization time-of-flight mass spectrometry (HR-MALDI-TOF), and UV−vis experiments (Figures S2−S22).

2.2. Electro-Optical and Physical Properties. The normalized absorption spectra of MPcs in solvents and solid films (Figure 2a,b) are displayed, and the stronger peak at the Q band was used as the standard for normalization. The Soret bands (B bands) are located in the ultraviolet region (300−430 nm), which is linked to the transitions from S_0 to S_2 (ground state to the second excited state). We attribute the appearance of a trivial shoulder at ∼615 nm to the vibronic band. Strong absorption (600−800 nm) suggests that the Q-band signal is related to the transition from S_0 to S_1 (ground state to the first excited state) and interpreted as $\pi-\pi^*$ excitation between bonding and antibonding molecular orbitals.

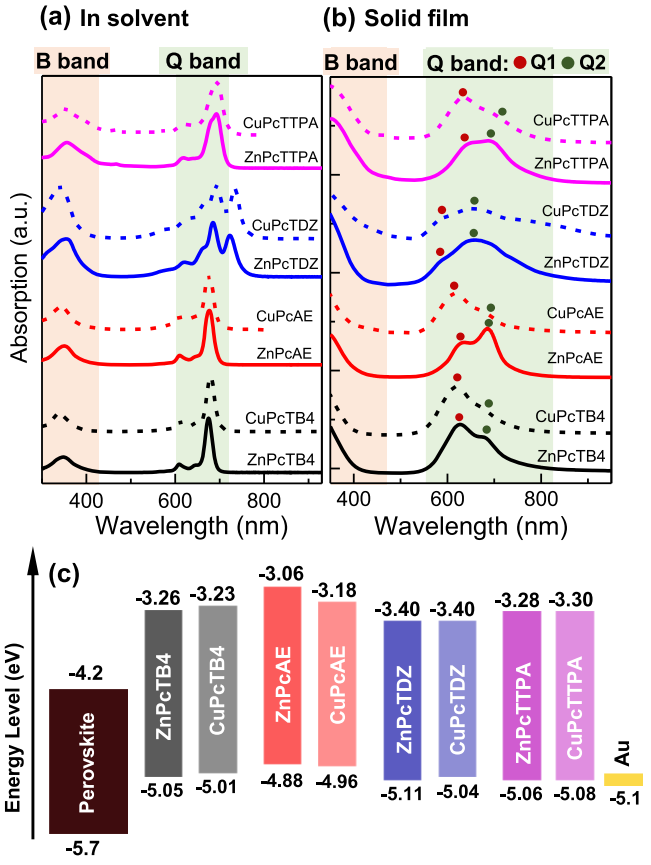

Figure 2. UV−vis absorption spectra of MPcs in (a) solution and (b) solid films and (c) energy level diagram for the hole-transporting side for all of the MPcs.

For the absorption spectra of the MPc in solvents, the Q band of MPcAE in the solvent is similar to that of MPcTB4 (Figure 2a), while the Q band of MPcTDZ and MPcTTPA split into doublet Q bands, which is attributed to the presence of different regioisomers and also by the breaking of the D_{4h} symmetry.[25] Besides, the Q band of MPcTDZ displays the widest absorbance from 500 to 785 nm and shows another band situated at 723 nm for ZnPcTDZ and 736 nm for CuPcTDZ because of the thiadiazole ring. The absorption spectra of MPcTTPA is bathochromically shifted compared to that of MPcTB4 and exhibited broadened absorption in contrast to that of MPcTB4.

The absorption spectra of the films on quartz (Figure 2b) display a spread of the signals from red and blue by comparing with the solution spectra (Figure 2a), and the absorption of MPc films displays wide Q bands from 550 to 800 nm. When compared with MPcTB4, a slight bathochromic shift is observed in MPc with other substitutions. This phenomenon can be related to the formation of aggregates, which can affect the charge carrier transport in the solid film.[26,27]

The peak absorption band at short wavelength named Q1 is attributed to the aggregated species and face-to-face stacking of the molecules, while the other peak absorption at long wavelength called Q2 is attributed to the monomeric species.[28] The primary species of MPcs were evaluated from the relative intensities of Q1 and Q2 bands. For ZnPcs, ZnPcTB4 holds the main aggregated species, but other ZnPcs possessed the main monomeric species. It illustrates that different substitutions can control the aggregation in the film and charge carrier transport. However, apart from CuPcTDZ with monomeric species, the other CuPcs show rich aggregated species.[28,29]

The asymmetrical MPcs with TDZ and TTPA substituents displayed distinct absorption in the solution, while MPcs with the AE group display similar absorption curves as of the reference (MPcTB4). Arguably, the optical properties of the new MPcs could be controlled by the asymmetrical substitution groups. Importantly, the primary species of MPcs in the solid films for asymmetrical ZnPcs is monomeric species, while in ZnPcTB4 is aggregated ones. In contrast, the trend of primary species in CuPcs is not in a similar fashion as ZnPcs, suggesting that the primary species can be tuned by the asymmetrical group and core metal synergistically.

To evaluate the energy level alignment of the perovskite/MPc interface, we performed electrochemical characterization using differential pulse voltammetry (Figures S23−S27) and ferrocene redox couple as the external standard (Table S1). The highest occupied molecular orbital energy levels (E_{HOMO}) were deduced from the equation: $E_{HOMO} = -4.8 - E_{ox}$, where E_{ox} is the first onset oxidation potential. The lowest unoccupied molecular orbital energy levels (E_{LUMO}) of MPcs were determined by adding the optical band gap to the E_{HOMO} value. The schematic diagram displays the energy level of perovskites (Figure 2c) and the energy levels of reported MPcs (ZnPcTB4, ZnPcAE, and ZnPcTDZ) noted from the literature. We noted that asymmetrical MPc with a similar substitution but with different core metals presents similar E_{HOMO} and E_{LUMO}, while different substitutions influence the semiconducting properties. The energy levels of the asymmetrical MPc with TDZ and TTPA show a trivial difference, but asymmetrical MPcAE has a slightly higher energy level

https://doi.org/10.1021/acsaem.1c02039
ACS Appl. Energy Mater. 2021, 4, 10124−10135

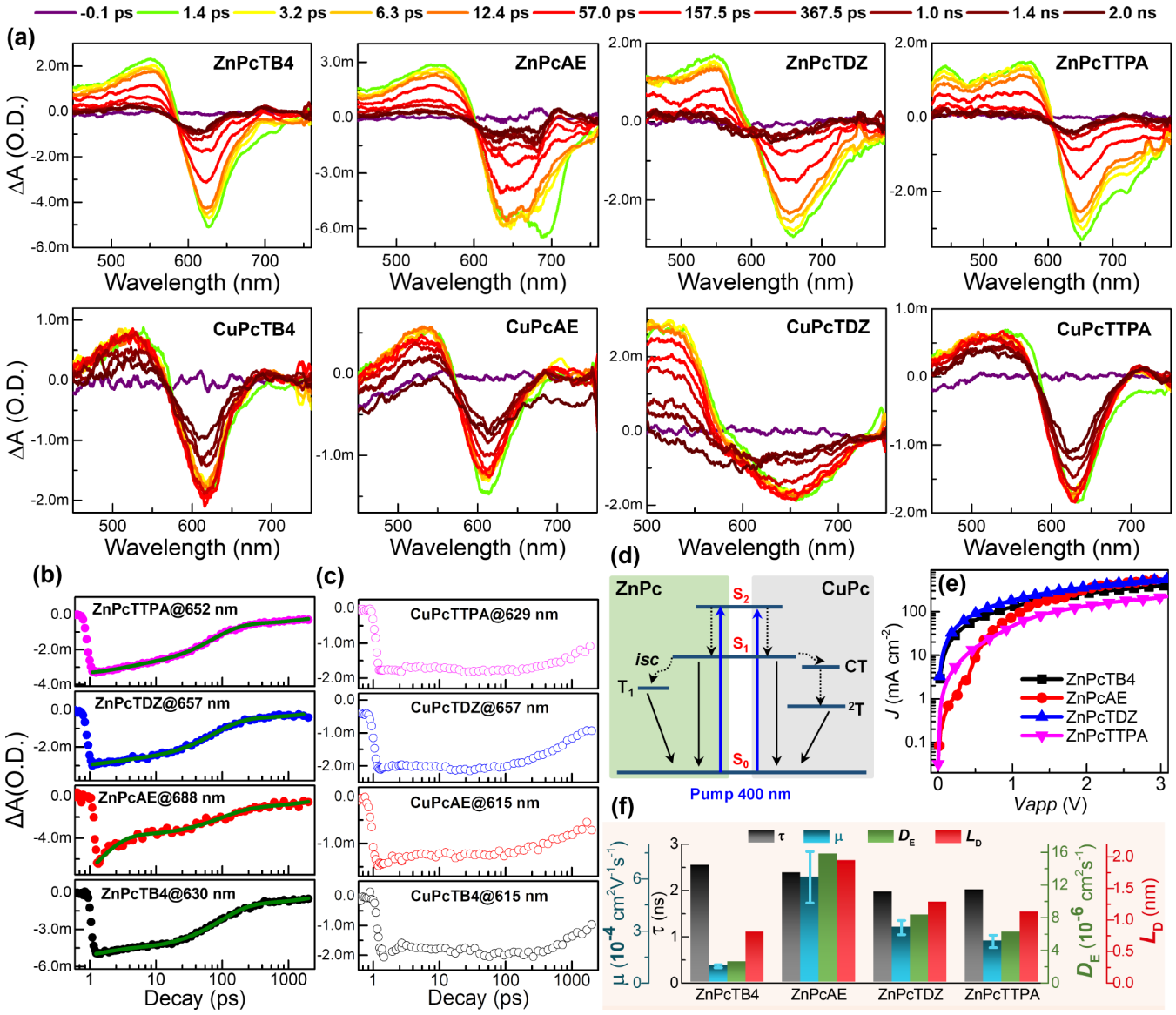

Figure 3. (a) TA spectra evolution of ZnPcs and CuPcs at indicated times (details in the legend). All of the samples were spin-coated on a quartz substrate. Kinetic traces of (b) ZnPcs and (c) CuPcs at the maxima GSB signal point, (d) schematic diagram of the energy relaxation dynamics of ZnPc and CuPc, (e) J–V curves of the ZnPc-based hole-only device with the structure: FTO/poly(3,4-ethylenedioxythiophene) poly(styrene sulfonate) (PEDOT:PSS)/HTM/Ag, and (f) summary of the charge transfer (CT) parameters of ZnPcs.

than the reference, which may be ascribed to aminoethoxy subtituent as end arms. Assuming that the valence band/conduction band of mixed-ion perovskites are at −5.7/−4.2 eV, all of the E_{HOMO} of MPcs are energetically favorable, signaling an efficient charge extraction at the interfaces. The E_{HOMO} of MPcTDZ lies lowest than that of other MPcs, thus a higher open-circuit voltage (V_{oc}) of the corresponding device can be expected. Owing to the narrow band gap of MPcs, the highest value is 1.82 eV for ZnPcAE, and the lowest value is 1.64 eV for CuPcTDZ. Arguably, the photogenerated electron will also be transported by MPcs and increase the interface recombination, while ZnPcAE with higher E_{LUMO} is potentially attractive to block the electron effectively as compared to others.[30]

2.3. Ultrafast Transient Absorption Studies. To unravel the carrier transport properties in these asymmetrical MPcs and probe their correlation with core metal and substitutions, we investigated the charge carrier dynamics of thin films via transient absorption spectroscopy (TAS). The TAS spectra (Figure 3a) in the visible range at the indicated delay times, presented a broad positive signal (peak) at the wavelength region between the B band and Q band, which is typically associated with the singlet and triplet excited-state absorption of photogenerated carriers or excitons in the film.[31,32] The broad negative signals (trough) at the wavelength region of the Q band is attributed to the overlapping between the ground-state bleaching (GSB) and the stimulated emission (SE) for Soret fluorescence, where the GSB is stemmed from the depletion of the population in the ground electronic state following photoexcitation. We noted the profile of TAS mismatch with the static absorption (Figure S28). All of the ZnPc samples display faster decaying on a picosecond timescale (10 ps) and near-complete decay reaching nanoseconds. However, the CuPcs present dissimilar decay phenomena except for CuPcAE, compared to Zn-based counterparts, CuPcTB4 showed a signal increase within

https://doi.org/10.1021/acsaem.1c02039
ACS Appl. Energy Mater. 2021, 4, 10124−10135

hundreds of picoseconds, but CuPcTDZ and CuPcTTPA presented no decay within this time frame (hundreds of picoseconds). The signal of all CuPcs showed only a half decay value reaching nanoseconds.

We investigated the dynamic traces of ZnPcs and CuPcs at the trough point (Figure 3b,c) to clarify the charge kinetic decay process. The three timescales can be distinguishably observed for ZnPcs: the first fast decay within the first few picoseconds can be ascribed to the intersystem crossing (i_{sc}) from ($S_1 \rightarrow T_1$) because the internal conversion ($S_2 \rightarrow S_1$) occurs within the femtosecond timescale. The other two components correspond to the repopulation of the ground state (S_0) including two branches: a substantial decay from the exciton state via exciton−phonon coupling ($S_1 \rightarrow S_0$) with hundred picoseconds and slow decay with nanoseconds via nonradiative relaxation of the triplet state ($T_1 \rightarrow S_0$). We draw a schematic diagram for MPcs illustrating the entire transient process (Figure 3d).

The traces of ZnPcs were well fitted with a triexponential function with the decay equation: $I(t) = \sum \alpha_i \exp(-t/\tau_i)$, where $I(t)$ is the total transient absorption decay curve, and α_i and τ_i are the relative amplitude and lifetime of the ith component (the normalization condition being $\sum_i \alpha'_i = 1$), respectively (Table S2). The range of the carrier lifetime is in agreement with the reported values.[33,34] The carrier lifetime for asymmetrical ZnPcs with different substitutes is similar to the reference (ZnPcTB4). However, ZnPcAE has the larger amplitude value (0.65) than ZnPcTB4 (0.21), ZnPcTDZ (0.12), and ZnPcTTPA (0.16). We attribute this discrepancy in the lifetime and amplitude to the stronger spin−orbit coupling effect introduced by substitution groups in asymmetrical ZnPcs.

All of the CuPcs showed longer relaxation kinetics than the Zn-based counterparts. The CuPcTB4 and CuPcAE samples showed faster relaxation within the first 2 ps. The Cu element (atomic number 29) has an unfilled d-orbital with an electronic configuration of $3d^9 4s^2$ in contrast to the Zn element (atomic number 30) that possessed a filled d-orbital with an electronic configuration of $3d^{10} 4s^2$, indicating that Cu-based Pcs achieve a higher probability of donor−acceptor interactions between the core Cu metal and peripheral groups.

The CuPc derivatives can be populated by relaxing their excited singdoublet state (^2S) through the ligand-to-metal charge transfer (CT) to a triplet (tripdoublet) state of ^2T with a sequential decay passage of $^2S_1 \rightarrow {}^2CT \rightarrow {}^2T$.[25,31,35] The decay process in CuPcs does not accept a direct flip of the electronic spin state,[31,36,37] which was evidenced to be more swift and efficacious than the decay process in ZnPcs, in which i_{sc} transition is accountable for the $S_1 \rightarrow T_1$ decay. Similar phenomena were reported in copper-based porphyrins and phthalocyanines.[31,37,38] Faster decay curves for CuPcTDZ and CuPcTTPA were not observed by us within the first 2 ps, and this can be explained mainly by the fast decay via CT and stimulated emission.

Unlike the signal of the corresponding ZnPcs at the maxima point showing a continuous decay, CuPc (TB4, TDZ, TTPA) shows no significant change in decay within the hundred picoseconds, and CuPcAE has slower decay than ZnPcAE. As referred above, the trough signal was controlled by GSB and SE, the absent decay or slower decay of CuPcs resulted from the stimulated emission. It indicates that the stimulated emission in CuPcs can increase the decay lifetime because of the unique electronic structure of Cu elements.[39,40] The decay curves' divergence of all CuPcs ascribed to that different substitution, which can affect the triplet process, probably originated from the improved molecular interaction and increase of the Forster energy transfer process, which lead to excitation coupling with $\pi \rightarrow \pi^*$ transitions between closed molecules.

For phthalocyanine, the energy relaxation process should make the signal eventually decay to zero at a more extended time decay. The strong GSB of CuPcs finally evolves into a long-lived process and does not finish their decay in our detection window (2.0 ns). We ascribed the longer lifetime in CuPcs to the strong spin−orbit coupling effect introduced by the Cu atom. The stimulated emission phenomena in CuPc are stronger than the corresponding ZnPcs, which can increase the lifetime of CuPcs.

In all, the core metals and different substitutions of the asymmetrical MPcs, the charge decay process is synergistically controlled in the solid film. The asymmetrical MPcs have no measurable influence on the lifetime of the decay process, their impact on the amplitude for the intersystem crossing by inhibiting molecular aggregation, playing a role in the donor/acceptor. Compared to Zn as the core metal, the Cu element with unfilled d-orbitals possesses a unique decay process ($^2S_1 \rightarrow {}^2CT \rightarrow {}^2T$) and increase decay via stimulated emission and has a longer lifetime. The asymmetrical MPcs and core metals can affect the triplet state properties that in turn influence the transportation of electrons and holes.

At the first instance, the longer τ_e of MPcs of triplet state excitons emerges to show viability for the increasing diffusion length (L_D) via the triplet sensitization pathway. On the contrary, the longer τ_e is offset for the significantly reduced diffusion coefficient (D_E), and the Forster resonance energy transfer for (pure) triplet state diffusion is spin-forbidden, while a Dexter energy transfer with a much shorter operating range will essentially take charge of the energy migration process.[41]

The hole mobility (μ) of ZnPcs was determined by space-charge-limited current measurement (Figure 3e), and the corresponding D_E was derived according to the Einstein relation with a classical equation: $D_E/\mu = kT/q$, where k is the Boltzmann coefficient, q is the charge of the electron or hole, and T is the measuring temperature. The average value of hole mobilities for ZnPcs follows the order: ZnPcAE (~6.10×10^{-4} $cm^2\ V^{-1}\ s^{-1}$) > ZnPcTDZ (~3.21×10^{-4} $cm^2\ V^{-1}\ s^{-1}$) > ZnPcTTPA (~2.4×10^{-4} $cm^2\ V^{-1}\ s^{-1}$) > ZnPcTB4 (~0.97×10^{-4} $cm^2\ V^{-1}\ s^{-1}$). The corresponding D_E of ZnPcs was calculated (Figure 3f and Table 1) and follows the order ZnPcAE (15.81×10^{-6} $cm^2\ s^{-1}$) > ZnPcTDZ (~8.32×10^{-6} $cm^2\ s^{-1}$) > ZnPcTTPA (6.22×10^{-6} $cm^2\ s^{-1}$) > ZnPcTB4 (2.52×10^{-6} $cm^2\ s^{-1}$). Although the Forster resonance energy transfer for pure triplet state diffusion is spin-forbidden, the highest amplitude of ZnPcAE for the i_{sc} process showed a substantial singlet character in its T_1 state and enhanced spin−

Table 1. Summary of the Charge Transfer Parameters of MPcs

HTM	τ_{ave} (ps)	μ (10^{-4} $cm^2\ V^{-1}\ s^{-1}$)	D_E (10^{-6} $cm^2\ s^{-1}$)	L_D (nm)
ZnPcTB4	2535.7	0.97	2.52	0.80
ZnPcAE	2380.0	6.10	15.81	1.94
ZnPcTDZ	1963.2	3.21	8.32	1.28
ZnPcTTPA	2005.1	2.40	6.22	1.12

https://doi.org/10.1021/acsaem.1c02039
ACS Appl. Energy Mater. 2021, 4, 10124−10135

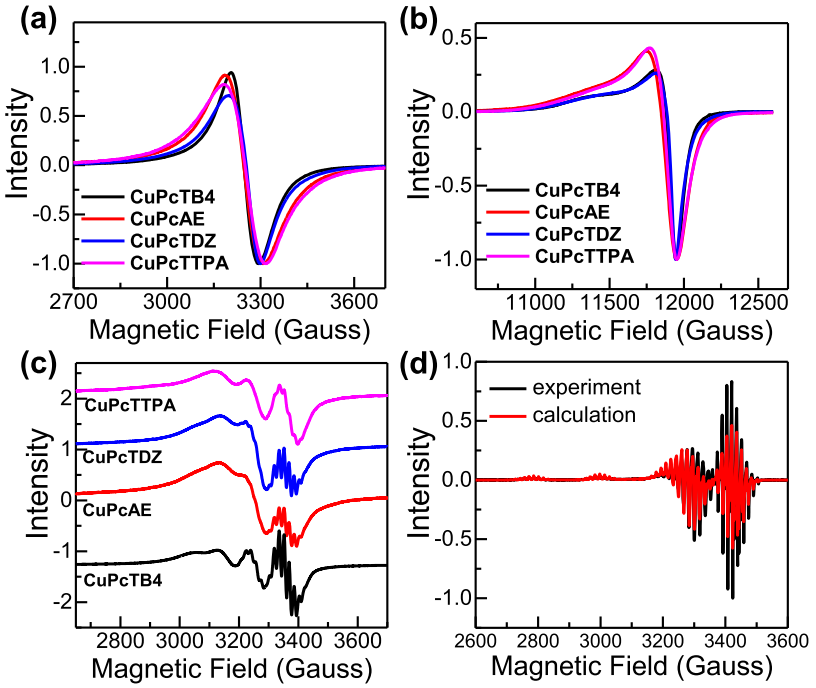

Figure 4. (a) X-band and (b) Q-band EPR spectra of CuPc solid samples at room temperature, (c) X-band room temperature EPR spectra of CuPc complexes dissolved in toluene, and (d) experimental and simulated EPR spectra of CuPcTB4 in toluene at 100 K.

orbit coupling. This is sufficient to enable Forster resonance energy transfer to occur. This singlet−triplet mixing could increase the μ and D_E and then L_D. The L_D of ZnPcs was thus calculated according to the equation $L_D = (D_E\tau)^{1/2}$, and the relevant parameters are summarized (Table 1). The L_D of ZnPcs showed the following order: ZnPcAE (1.94 nm) > ZnPcTDZ (1.28 nm) > ZnPcTTPA (1.12 nm) > ZnPcTB4 (0.80 nm). Longer L_D can improve charge transportability via inhibiting the carrier recombination induced by their narrow band gap in the transporting layer and thus boost the higher efficiency.

To establish the variation in electrical properties of ZnPcs with different substitutions, molecular orientation and the microstructure of MPcs were investigated. The grazing incidence X-ray diffraction (GIXRD) pattern was measured on FTO and perovskite-coated Pc substrates (Figure S29). The ZnPcs with substitutions showed no peak in the GIXRD patterns, indicating the amorphous nature. We investigated the film-forming ability of ZnPcs with the aid of scanning electron microscopy (SEM) and atomic force microscopy (AFM) (Figure S30) techniques. The uniform and fine coverage of perovskite layers with symmetrical ZnPc suggest its film-forming ability.

2.4. Electron Paramagnetic Resonance. To probe the possible interaction and relationship between the electronic structure of the phthalocyanine metal center and its photovoltaic performance, we recorded the electron paramagnetic resonance (EPR) spectra of the isostructural copper compounds.

The X-band room temperature EPR spectra of CuPcTB4, CuPcAE, CuPcTDZ, and CuPcTTPA solid samples show quasi-isotropic signals, centered about $g = 2.07$. We noted that neither the shape nor the position of the signal showed any noticeable changes, and a clear variation of the peak-to-peak linewidth was observed in the order: CuPcTB4 < CuPcTDZ < CuPcAE < CuPcTTPA. The Q-band spectra are better resolved showing the axial g anisotropy characteristic of copper(II) phthalocyanine complexes (Figure 4a,b).[42−46] The g values are obtained by simulation of the experimental spectra (Table S3). In all of the cases, the lowest g deviates significantly from the free-electron value ($g_e = 2.0023$) and $g_\parallel$ is higher than $g_\perp$, thus the unpaired electron occupies the $d_{x^2-y^2}$ orbital in the equatorial plane of a Cu(II) chromophore with elongated tetragonal symmetry. The calculated g values are in agreement with those observed in other CuPc complexes.[44,45] The absence of a resolved copper and nitrogen hyperfine structure is due to dipolar and/or exchange interactions between Cu(II) ions from different molecules.

To elucidate if the g values obtained from the solid-state experiments are molecular, we also investigated using the G parameter proposed by Hathaway [$G = (g_\parallel - 2)/(g_\perp - 2)$] which lies in the 4.4−4.9 range when the g values are equal to molecular values.[47] In this case, G is close to 3 for all of the compounds, which implies that the g values are averaged due to spin−spin interactions. In this context, the smaller peak-to-peak linewidth observed in the EPR spectra of CuPcTB4 implies that the exchange interactions in this solid are more efficient than those in the other complexes.

To reduce the spin−spin interactions, to improve the resolution of the EPR signal, and to derive further information over the effects of the substitution of peripheral ligands on the electronic structure and bonding, the copper complexes were dissolved in toluene. In all of the cases, the X-band solution of EPR spectra recorded at room temperature (Figure 4c) show four hyperfine lines due to the interaction of Cu(II) unpaired electrons with the copper nuclei ($I = 3/2$, isotopes ^{63}Cu and ^{65}Cu). Besides, a super hyperfine splitting due to the presence of four geometrically equivalent ^{14}N nuclei ($I = 1$) can be observed. Moreover, the line widths show the typical dependence with the nuclear quantum number M_I ($\Gamma = \alpha + \beta M_I + \gamma M_I^2$)[48] due to molecular tumbling effects, with better resolution on the $M_I = +1/2$ and $+3/2$ lines, especially for the

https://doi.org/10.1021/acsaem.1c02039
ACS Appl. Energy Mater. 2021, 4, 10124−10135

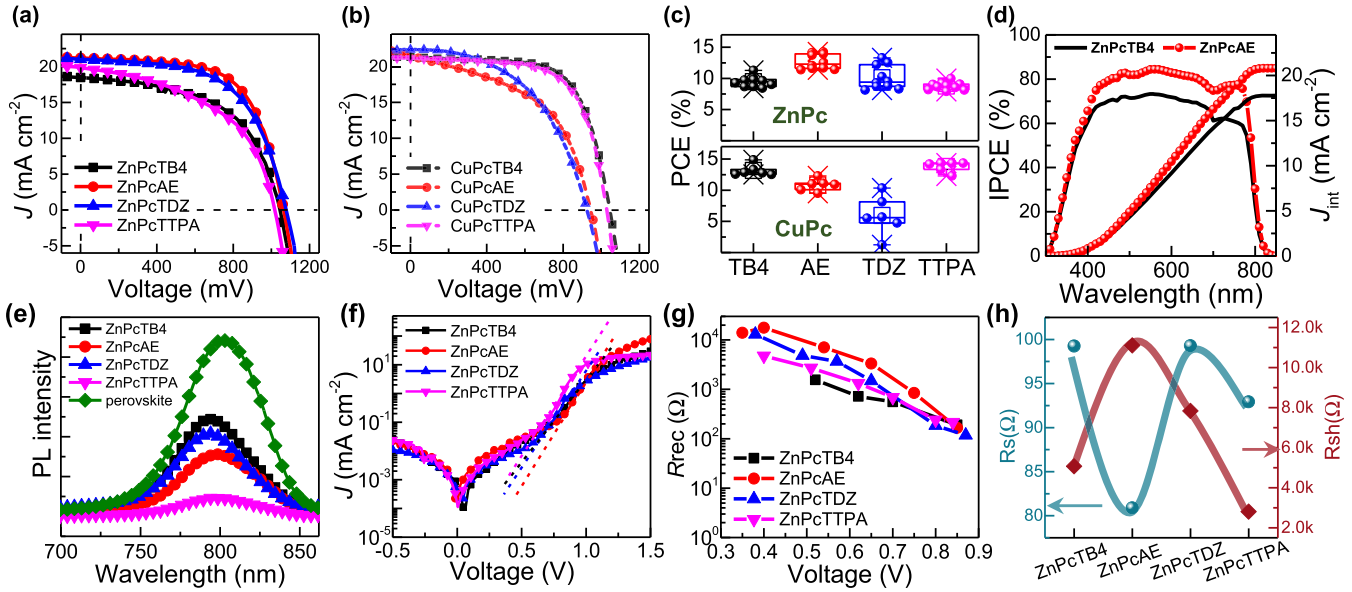

Figure 5. $J-V$ curves of the champion device with different (a) ZnPcs and (b) CuPcs as the HTM and b&mp-TiO_2 as an ETM, (c) statistical efficiency performance of PSCs with ZnPc and CuPc HTMs. The average values were analyzed from 10 devices for ZnPcs-based PSCs and 6 devices for CuPc-based PSCs, (d) IPCE and integrated J_{int} of the device with ZnPcTB4 and ZnPcAE as HTMs respectivley, (e) steady-state photoluminescence (PL) spectra of bare perovskite and perovskite with different ZnPc HTMs, and (f) $J-V$ curves in the dark (the dashed−dotted lines present the fitting lines for J_0 and n). (g) Recombination resistance extracted from the impedance spectra plots for the device with different ZnPcs under different photovoltages. (h) R_s and R_{sh} values extracted from champion $J-V$ urves of the device with different ZnPcs measured under a reverse scan.

CuPcTB4 compound. Considering that the concentration of spins was similar in all solutions, the main causes of the different resolutions observed for each compound must be the molecular tumbling. The tumbling coefficients depend on the anisotropies of g and of the hyperfine couplings and on the rotational rate.[44] By simulation of the room temperature solution spectra (Figure S31), the isotopic values of g, A_{Cu}, and A_N (Table S4) have been determined, showing that within the experimental uncertainty the electronic distribution around Cu(II) ions is similar for all of the studied compounds. When the molecular rotation is stopped upon freezing, all of the spectra become analogous. Arguably, the replacement of ligands carried out mainly affects the motional behavior of the complexes.

Finally, the X-band EPR spectrum of a frozen toluene solution of CuPcTB4 (Figure 4d) was simulated to determine the principal values of the g, A_{Cu}, and A_N tensors. We fitted the spectrum by taking into consideration the presence of two resonant species, one containing ^{63}Cu and the other ^{65}Cu, both in their natural abundance (69.15 and 30.85%, respectively). The derived parameters (Table S4) confirm the D_{4h} symmetry around the copper(II) ions in this compound as well as a considerable delocalization of the d electrons over the isoindole nitrogens.

As compared to the reference (CuPcTB4), the asymmetrical CuPc has a dissimilar electronic structure. However, it signals unique solid-state magnetic exchange, i.e., the packing of the molecules and thus the $\pi-\pi$ interactions and the energy of the frontier orbitals. These results follow the results of transient absorption, which suggest that asymmetric substitutions show different lifetimes of excited-state relaxation.

2.5. Photovoltaic Performance of PSCs with ZnPcs as HTMs. To elucidate the significance of different substitutions and core metals on the performance of PSCs, we fabricated PSCs with the architect of FTO/b&mp-TiO_2/perovskite/Pcs/Au (b&mp-TiO_2: compact and mesoporous TiO_2 layers). The schematic of the PSCs and the cross-sectional SEM image of the device with ZnPcAE as an HTM (Figure 1) display a well-defined layer-by-layer structure with sharp interfaces. The perovskite ($FA_{1-y}MA_yPbI_{3-x}Br_x$) layer was prepared by a two-step deposition method ($t \sim 500$ nm), while ZnPcAE was spin-cast on the perovskite layer to serve as an HTM ($t \sim 112$ nm).

First, chloroform and chlorobenzene were probed to investigate the effect of solvents on the charge transport performance of ZnPcAE. The film deposited by the chloroform solvent shows better PV performance than chlorobenzene (Figure S32), and to decipher this, we analyzed the microstructure systematically. The UV−vis absorption of ZnPcAE deposited in different solvents gave a similar peak and absorption intensity. We examined the surface microstructure of the perovskite coated with ZnPcAE derived from different solvents (Figure S33). The film deposited by chlorobenzene displays undissolved solids on the surface, which will promote recombination centers and reduce the charge extraction abilities. The root-mean-square roughness (RMS) of perovskite/ZnPcAE prepared by chlorobenzene with ∼17.2 nm is higher than that prepared by chloroform and signals uniformity and smoothness, which in turn will allow building the sharper interface for efficient hole transportation.

The $J-V$ curves of the device using different HTMs are shown (Figure 5a,b) and the corresponding photovoltaic parameters are listed (Table 2). For the device with ZnPc as HTMs, the device employing ZnPcTB4 exhibits a PCE of only 10.52% with a V_{oc} of 1042.6 mV, J_{sc} of 18.46 mA cm^{-2}, and fill factor (FF) of 54.7%. Interestingly, after substitutions with other groups, all compounds show better device performance. Especially, the ZnPcAE HTM exhibit the highest PCE with 14.25% with a V_{oc} of 1063.5 mV, J_{sc} of 21.19 mA cm^{-2}, and FF of 63.2%, which mainly resulted from the enhanced J_{sc} and FF. The average of PCE from the device with different HTMs

https://doi.org/10.1021/acsaem.1c02039
ACS Appl. Energy Mater. 2021, 4, 10124−10135

Table 2. Champion Photovoltaic Parameters of the PSCs Based on Different MPcs

HTM	V_{oc} (mV)	J_{sc} (mA cm^{-2})	FF (%)	PCE (%)
ZnPcTB4	1042.6	18.46	54.7	10.52
ZnPcAE	1063.5	21.19	63.2	14.25
ZnPcTDZ	1076.3	21.02	58.8	13.30
ZnPcTTPA	1016.6	19.83	49.5	9.97
ZnPcAE[a]	974.3	24.35	65.8	15.61
CuPcTB4	1044.9	21.29	66.9	14.87
CuPcAE	915.7	22.66	59.2	12.29
CuPcTDZ	925.2	22.32	50.1	10.34
CuPcTTPA	1028.8	21.14	66.0	14.35

[a]PSC based on b-TiO_2/SnO_2 as the ETM and the rest are with b&mp-TiO_2 as the ETM.

show a similar trend (Figure 5c and Table S5). The J_{sc} values match with integrated current densities (20.8 mA cm^{-2}) obtained from the incident photon-to-current conversion efficiency (IPCE) (Figure 5d), indicating that ZnPcAE exhibits a higher photon-to electron conversion efficiency than ZnPcTB4 for the whole visible wavelength region. The V_{oc} of ZnPcTDZ presents the highest values compared with other ZnPcs, which originated from the well-matched energy level. For the Zn-based Pcs, ZnPcAE (1.94 nm) and ZnPcTDZ (1.28 nm) possessed higher L_D than ZnPcTB4 (0.80 nm) and ZnPcTTPA (1.12 nm), respectively, and thus yield a higher efficiency than ZnPcTB4/ZnPcTTPA.

We optimize the device performance of ZnPc-based PSCs by replacing mp-TiO_2 with planar SnO_2 quantum dots as an ETM, reaching a PCE of 15.61% with V_{oc} of 974.2 mV, J_{sc} of 24.35 mA cm^{-2}, and an FF of 65.79% (Figure S34). We attribute this to SnO_2 unique properties such as higher conductivity and optical transparency compared to mp-TiO_2. We investigated the hysteresis index (HI) in champion devices by measuring $J-V$ curves under the forward and reverse scan directions. The devices with ZnPcAE and ZnPcTDZ have quite small HI values of 0.09 and 0.07, respectively (Figure S35 and Table S6).

On the other hand, considering the results of the PV device with ZnPcs, the device with CuPc analogues as HTMs should have a similar trend as of ZnPcs; however, they are dissimilar to the ZnPcs. The device with CuPcTB4 and CuPcTTPA yields higher efficiency than that of CuPcAE and CuPcTDZ. The device with CuPcTB4 and CuPcTTPA exhibits the highest PCEs of 14.87 and 14.35%, higher than CuPcAE and CuPcTDZ with 12.29 and 10.34%, respectively. We noted the difficulties in depositing uniform films for CuPcAE and CuPcTDZ. Although solvent engineering included chloroform/methanol mixed solvents for CuPcAE and the chlorobenzene/tetrahydrofuran mixed solvent for CuPcTDZ, the corresponding efficiency is lower. The device with CuPcs (CuPcTB4, CuPcTTPA) shows higher efficiency than that of the device with Zn-based counterparts. The CuPcs possessed a higher efficiency than the Zn-based counterparts, which can result in the higher charge transporting ability that originated from their long lifetime. Considering the solubility issues with CuPcs, the discrepancy in device performance is difficult to correlate with their transportability. We investigated the carrier transportation difference employing ZnPc HTMs.

Steady-state photoluminescence (PL) measurement for perovskites using different ZnPcs with the film structure of quartz/perovskite/ZnPc was used to analyze the charge carrier transport process (Figure 5e). An emission peak centered at 803 nm for the pristine perovskite was observed. A reduced PL intensity was recognized for all of the ZnPcs, indicating efficient hole carrier extraction from perovskite. Remarkably, a blue-shifted PL peak was observed for all of the perovskite/ZnPcs, which can be ascribed to a decrease in the bulk and/or surface trap states in the perovskite layer after the deposition of a thin layer of HTM.[49] ZnPcAE and ZnPcTDZ showed a large blue shift compared to the other one, consequently, they showed lesser charge recombination at the interface between the perovskite and HTM layers measured by electrical impedance spectroscopy (EIS) and dark $J-V$ measurements indicating a low value of the reverse saturation current, as discussed in the section below. Subsequently, we noted improved PCE, due to enhancement in the open-circuit voltage (V_{oc}) and short-circuit current.

To evaluate the function of different ZnPc HTMs on the performance of the PSCs, dark current was measured (Figure 5f), the linear parts of the dark $J-V$ curves were fitted with the Shockley diode equation: $J_D = J_0[\exp(qV/nK_BT) - 1]$, where J_0 is the reverse saturation current density, J_D is the dark current density, V is the applied bias, q is the electron charge, K_B is the Boltzmann constant, T is the temperature, and n is the ideal factor of the real diode.[50,51] For devices with different ZnPcs as HTMs, n, and J_0 are listed in Table S7. The values of [n, J_0] was [2.94, 5.5 × 10^{-6} mA cm^{-2}], [2.3, 1.4 × 10^{-7} mA cm^{-2}], [2.6, 2.2 × 10^{-6} mA cm^{-2}], and [2.4, 2.4 × 10^{-6} mA cm^{-2}] for the PSCs based on ZnPcTB4, ZnPcAE, ZnPcTDZ, and ZnPcTTPA, respectively. The smaller value of n and J_0 indicates a decrease in charge recombination at the interface between the perovskite and HTM layers. Thus, it is revealed that ZnPcAE reduces interface recombination and improves the transfer efficiency of the charge in the device and leads to the high FF of the corresponding device.

To elucidate the charge transport kinetics (surface recombination, charge carrier diffusion, etc.) in devices based on developed ZnPcs, electrical impedance spectroscopy (EIS) was measured under different light intensities (0−0.2 Sun) of white light-emitting diode (LED) illumination to produce different photovoltages.[52] An equivalent circuit was proposed ($R - R_{rec}/C$, Figure S37) to interpret the interface recombination. R is seen as the series resistance of the external circuit including connecting wires and two electrodes, and R_{rec} reflects the impact of recombination resistance of the device. In the typical Nyquist diagram of different devices with varying photovoltages (Figure S38), only R_{rec} values under a series of photovoltages from different ZnPc-based devices were extracted and plotted (Figure 5h) for discussion. With the increase in photovoltages, the value of R_{rec} decreases, due to the improvement in carrier concentration. At a similar potential bias, the R_{rec} values of the ZnPcAE-based device are beyond the values from other devices, which implies that ZnPcAE steeply reduced charge recombination at the perovskite/HTM interface.

The series resistance (R_s) and shunt resistance (R_{sh}) of devices were derived by fitting the $J-V$ curves measured in the reverse scan (Figure 5i). The ZnPcAE-based PSCs showed the lowest R_s of 81 Ω, whereas ZnPcTB4, ZnPcTDZ, and ZnPcTTPA-based- PSCs displayed the R_s of 99, 99, and 92 Ω, respectively. Moreover, the ZnPcAE-based device possessed the highest R_{sh} of 11.1 kΩ, whereas ZnPcTB4, ZnPcTDZ, and ZnPcTTPA-based devices showed the R_{sh} of 5.1, 7.8, and 2.8 kΩ, respectively. The abilities to transport charge effectively

https://doi.org/10.1021/acsaem.1c02039
ACS Appl. Energy Mater. 2021, 4, 10124−10135

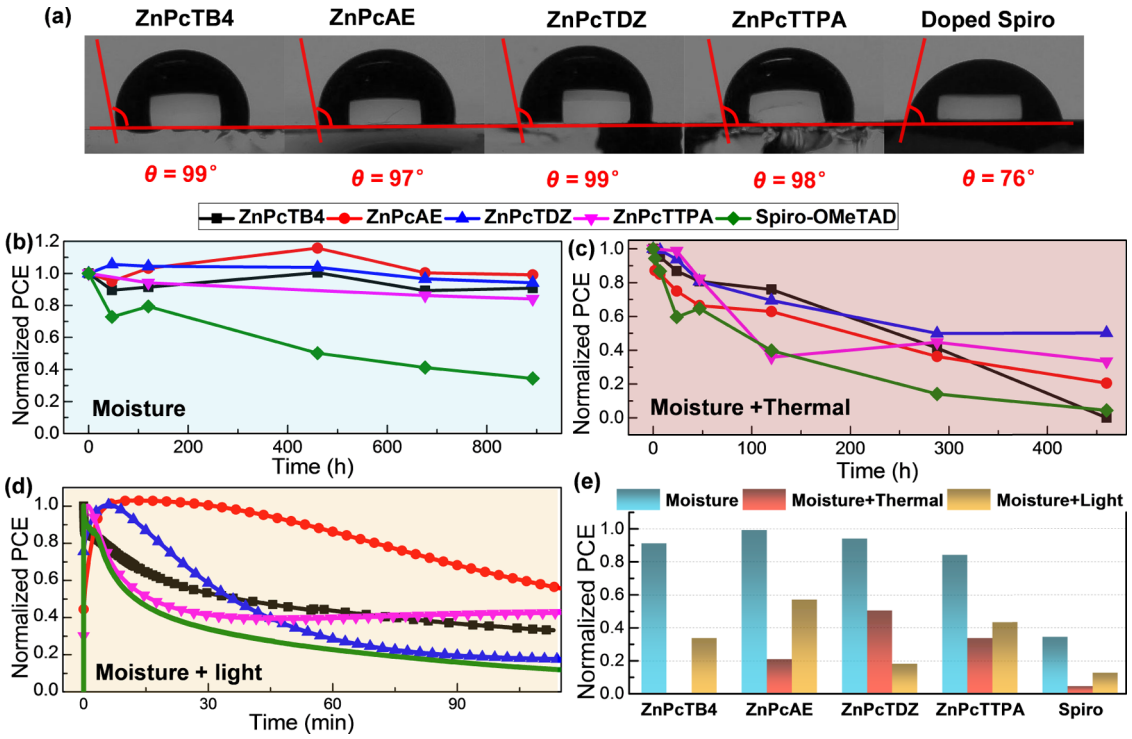

Figure 6. (a) Contact angles of perovskite with different ZnPcs and Spiro-OMeTAD, (b) PCE plots of PSCs with different ZnPcs and Spiro-OMeTAD aged under ambient conditions (30−70% RH) for around 900 h, (c) plots of efficiency of PSCs based on different ZnPc and Spiro-OMeTAD HTMs under moisture and heat conditions, (d) maximum power point tracking under moisture and 1 sun illumination of the unencapsulated device with different HTMs, and (e) normalized PCE obtained after aging conditions. (Spiro: Spiro-OMeTAD).

are decisive for their performance of PSCs and the electrical conductivity for HTMs (Figure S36) was measured. The trend of R_{sh} is in agreement with the R_{rec}. The conductivity value in our condition follows the order: ZnPcAE (0.22 μS cm^{-1}) > ZnPcTDZ (0.19 μS cm^{-1}) > ZnPcTTPA (0.15 μS cm^{-1}) > ZnPcTB4 (0.08 μS cm^{-1}). Overall, the lowest R_s and highest R_{sh} of the ZnPcAE-based device yielded improved PCE with higher FF, which is ascribed to the relatively higher conductivity.

2.6. Device Stability Performance. In addition to PSC performance, reliability is the crucial aspect to evaluate the performance of HTMs. To evaluate the surface nature, goniometer experiments were made to evaluate the hydrophobicity of perovskite films coated with different ZnPcs. The contact angles showed 99, 97, 99, and 98°, respectively, after spin-coating ZnPcTB4, ZnPcAE, ZnPcTDZ, and ZnPcTTPA atop the perovskite (Figure 6a), while that of the perovskite with doped Spiro-OMeTAD is 75°. The perovskite-coated ZnPc samples yielded a contact angle over 90° and perovskite/ZnPcAE gave the highest value among them. The hydrophobic properties induced by ZnPcs can effectively prevent water from diffusing into the perovskite layer, thus leading to enhanced moisture stability. The substituted groups in asymmetrical ZnPcs also influence the surface properties marginally.

For reliability purposes, the PSCs should operate under combined stress conditions instead of only one factor. To evaluate the potential of ZnPc-based PSCs, we investigated the stability of PSCs with ZnPcs under various stress conditions. First, we measured the unencapsulated PSCs under the ambient conditions with 30−70% relative humidity (RH), around 900 h (Figure 6b). The PCE based on ZnPcTB4, ZnPcAE, ZnPcTDZ, and ZnPcTTPA can retain 91, 99, 94, and 84% of their initial PCE after aging, respectively, while the control device employing doped Spiro-OMeTAD as an HTM yielded around 17% (Figure S39) and lost 70% of its initial PCE. The detailed PV parameters containing V_{oc}, J_{sc}, and FF are shown (Figure S40). The J_{sc} values of ZnPc-based PSCs remain unchanged, suggesting that the perovskite can maintain the role as an active layer, but the J_{sc} value of the control device decreases to 50% of its initial value. UV−vis absorption spectra to study the degradation process of perovskites with different HTMs were recorded at 550 nm wavelength vs time (Figure S41a). The perovskite with ZnPcs retains 80% absorbance of its initial values, while perovskite/Spiro-OMeTAD holds only 60% of the initial value. The visual image of perovskite layers with different HTMs after aging around 900 h was documented (Figure S41b). Perovskite/Spiro-OMeTAD displayed a brown color instead of an intense dark color, suggesting degradation of the phase change. However, perovskites with ZnPcs showed a dark color, indicating the entirety of the perovskite with ZnPcs, which is consistent with the PV performance. The FF value is related to the series resistance and ZnPc-based PSCs retain >95% of their initial values after aging, suggesting that ZnPcs create the rational interface between ZnPcs and perovskites. However, the R_s value is 3-fold in the case of the control device (Figure S41c), suggesting that both the intrinsic poor stability of doped Spiro-OMeTAD and the decomposition of the perovskite-induced dopant (lithium salt and *t*-BP) in Spiro-OMeTAD deteriorate the perovskite/HTM interface and the active layer.

Second, the devices were exposed to both environmental stress conditions (heat and humidity). The PV performance of PSCs was recorded under continuous thermal stress (85 °C) and ambient conditions with 30−70% RH for around 500 h

https://doi.org/10.1021/acsaem.1c02039
ACS Appl. Energy Mater. 2021, 4, 10124−10135

(Figure 6c), The PCE held 20, 50, and 33% of the initial value in the case of a device with ZnPcAE, ZnPcTDZ, and ZnPcTTPA, respectively, but nearly 0% of the initial value was noted for ZnPcTB4 and Spiro-OMeTAD-based PSCs. We noted that ZnPcAE, ZnPcTDZ, and ZnPcTTPA showed competitive performance when exposed to heat and high humidity conditions. The rate of change of J_{sc} and FF for ZnPcAE, ZnPcTDZ, and ZnPcTTPA-based PSCs was lower than that of ZnPcTB4 and the control device (Figure S42). The change in R_s calculated by fitting the $J-V$ curves as a function of time (Figure S41d), for ZnPcAE, ZnPcTDZ, and ZnPcTTPA-based PSCs displayed increments to 3.0, 1.5, and 2.6 times of its initial values, respectively, while the control device exhibited 24 times of the initial value, which has a negative influence on the device performance, especially J_{sc} and FF values. The Spiro-OMeTAD doped with the lithium salt and *t*-BP undergoes morphological deformation at a relatively high temperature and produced large voids.[53] Besides, the photo-oxidation induced in an oxygen-rich environment and the crystallization and the aggregate formation of Spiro-OMeTAD deteriorate its transporting properties.[54] The poor performance of ZnPcTB4 under heat stress originates from an anchoring group that does not interact with the perovskite layer judiciously, while other asymmetrical phthalocyanines can passivate the perovskite.

Further, we conducted maximum power point tracking of the unencapsulated devices under moisture (30−70% RH) with constant 1 sun illumination offered by a white LED at room temperature (Figure 6d). The control device drastically drops to 11% of its initial value after 118 min. However, the device with ZnPcTB4, ZnPcAE, ZnPcTDZ, and ZnPcTTPA maintained 33.4, 56.8, 17.7, and 43.1% of their initial PCE, respectively. ZnPcs, especially ZnPcAE possess excellent stability under humidity and light. The performance of the PSCs with different HTMs under stress conditions (Figure 6e) suggests that dopant-free ZnPcAE yielded improved stability as compared to ZnPc and traditional Spiro-OMeTAD.

3. CONCLUSIONS

We designed and quantified the physicochemical properties of a series of asymmetrical MPcs based on MPcTB4 (M = Zn or Cu) with AE, TDZ, and TTPA substituents and their influence on electro-optical and photovoltaic properties. The charge carrier dynamics of MPcs suggest a comparable average lifetime in ZnPc for varied substitutions, while CuPcs possess a longer lifetime than the Zn-based analogue. However, the ZnPcs signal a substantial difference in the amplitude, which can lead to an ample singlet character in the T_1 state. This, in turn, impacts the charge transport parameters such as mobility and the diffusion length of ZnPcAE, which are higher than those of similar ZnPcs. which is favorable for charge carrier extraction and transport in perovskite-based devices. The fabricated perovskite solar cells with ZnPcAE as the hole selective layer gave a competitive photovoltaic performance in its pristine form. Notably, the devices showed significant stability under multistress conditions.

■ ASSOCIATED CONTENT

Supporting Information

The Supporting Information is available free of charge at https://pubs.acs.org/doi/10.1021/acsaem.1c02039.

Materials and detailed synthesis and the corresponding characterization such as FT-IR, NMR, HR-MALDI-TOF, and cyclic voltammetry for all novel developed materials; additional experimental details for device fabrication and characterizations; experimental details for transient absorbance spectroscopy and electron paramagnetic resonance; GIXRD patterns of ZnPc on different substrates, morphological analysis of perovskite/ZnPc films; experimental and simulated X-band EPR; solvent optimization for ZnPcAE HTM; device performance of ZnPcAE and ZnPcTDZ, and Spiro-OMeTAD HTM; Nyquist curves for devices with different ZnPc HTMs; additional stability performance under different conditions; and additional table for CV and fitting parameters for ZnPc's curves, spin Hamiltonian parameters, and average PV parameters (PDF)

■ AUTHOR INFORMATION

Corresponding Authors

Ángela Sastre-Santos − *Miguel Hernandez University of Elche, 03202 Elche, Spain;* orcid.org/0000-0002-8835-2486; Email: asastre@umh.es

Shahzada Ahmad − *BCMaterials, Basque Center for Materials, Applications and Nanostructures, 48940 Leioa, Spain; IKERBASQUE, Basque Foundation for Science, 48013 Bilbao, Spain;* orcid.org/0000-0002-1218-2556; Phone: +34 946128811; Email: shahzada.ahmad@bcmaterials.net

Authors

Peng Huang − *BCMaterials, Basque Center for Materials, Applications and Nanostructures, 48940 Leioa, Spain*

Adrián Hernández − *Miguel Hernandez University of Elche, 03202 Elche, Spain*

Samrana Kazim − *BCMaterials, Basque Center for Materials, Applications and Nanostructures, 48940 Leioa, Spain; IKERBASQUE, Basque Foundation for Science, 48013 Bilbao, Spain*

Jorge Follana-Berná − *Miguel Hernandez University of Elche, 03202 Elche, Spain*

Javier Ortiz − *Miguel Hernandez University of Elche, 03202 Elche, Spain*

Luis Lezama − *Departamento de Química Orgánica e Inorgánica, Facultad de Ciencia y Tecnología, Universidad del País Vasco, 48940 Leioa, Spain;* orcid.org/0000-0001-6183-2052

Complete contact information is available at: https://pubs.acs.org/10.1021/acsaem.1c02039

Author Contributions

⊥P.H. and A.H. contributed equally to this work.

Notes

The authors declare no competing financial interest.

■ ACKNOWLEDGMENTS

This work received funding from the European Union H2020 Programme under a European Research Council Consolidator grant [MOLEMAT, 726360]. The authors gratefully acknowledge the financial support provided by the European Regional Development Fund "A way to make Europe and the Spanish Ministerio de Ciencia e Innovacion, Agencia Estatal de Investigación": project CTQ2017-87102-R AEI/FEDER, UE.

P.H. acknowledges funding from the European Commission via the Marie-Skłodowska-Curie Individual Fellowship (SMILIES, No. 896211).

REFERENCES

(1) NREL Best Research-Cell Efficiencies, 2021. https://www.nrel.gov/pv/cell-efficiency.html.
(2) Haris, M. P. U.; Kazim, S.; Pegu, M.; Deepa, M.; Ahmad, S. Substance and shadow of formamidinium lead triiodide based solar cells. *Phys. Chem. Chem. Phys.* **2021**, *23*, 9049−9060.
(3) Kojima, A.; Teshima, K.; Shirai, Y.; Miyasaka, T. Organometal Halide Perovskites as Visible-Light Sensitizers for Photovoltaic Cells. *J. Am. Chem. Soc.* **2009**, *131*, 6050−6051.
(4) Ponseca, C. S.; Savenije, T. J.; Abdellah, M.; Zheng, K.; Yartsev, A.; Pascher, T.; Harlang, T.; Chabera, P.; Pullerits, T.; Stepanov, A.; Wolf, J.-P.; Sundström, V. Organometal Halide Perovskite Solar Cell Materials Rationalized: Ultrafast Charge Generation, High and Microsecond-Long Balanced Mobilities, and Slow Recombination. *J. Am. Chem. Soc.* **2014**, *136*, 5189−5192.
(5) Stranks, S. D.; Eperon, G. E.; Grancini, G.; Menelaou, C.; Alcocer, M. J. P.; Leijtens, T.; Herz, L. M.; Petrozza, A.; Snaith, H. J. Electron-Hole Diffusion Lengths Exceeding 1 Micrometer in an Organometal Trihalide Perovskite Absorber. *Science* **2013**, *342*, 341−344.
(6) Salado, M.; Andresini, M.; Huang, P.; Khan, M. T.; Ciriaco, F.; Kazim, S.; Ahmad, S. Interface Engineering by Thiazolium Iodide Passivation Towards Reduced Thermal Diffusion and Performance Improvement in Perovskite Solar Cells. *Adv. Funct. Mater.* **2020**, *30*, No. 1910561.
(7) Huang, P.; Yuan, L.; Zhang, K.; Chen, Q.; Zhou, Y.; Song, B.; Li, Y. Room-Temperature and Aqueous Solution-Processed Two-Dimensional TiS 2 as an Electron Transport Layer for Highly Efficient and Stable Planar n−i−p Perovskite Solar Cells. *ACS Appl. Mater. Interfaces* **2018**, *10*, 14796−14802.
(8) Huang, P.; Wang, Z.; Liu, Y.; Zhang, K.; Yuan, L.; Zhou, Y.; Song, B.; Li, Y. Water-Soluble 2D Transition Metal Dichalcogenides as the Hole-Transport Layer for Highly Efficient and Stable p-i-n Perovskite Solar Cells. *ACS Appl. Mater. Interfaces* **2017**, *9*, 25323−25331.
(9) Huang, P.; Chen, Q.; Zhang, K.; Yuan, L.; Zhou, Y.; Song, B.; Li, Y. 21.7% Efficiency Achieved in Planar n-i-p Perovskite Solar Cells via Interface Engineering with Water-Soluble 2D TiS2. *J. Mater. Chem. A* **2019**, *7*, 6213−6219.
(10) Urbani, M.; de la Torre, G.; Nazeeruddin, M. K.; Torres, T. Phthalocyanines and Porphyrinoid Analogues as Hole- and Electron-Transporting Materials for Perovskite Solar Cells. *Chem. Soc. Rev.* **2019**, *48*, 2738−2766.
(11) Calió, L.; Kazim, S.; Grätzel, M.; Ahmad, S. Hole-Transport Materials for Perovskite Solar Cells. *Angew. Chem., Int. Ed.* **2016**, *55*, 14522−14545.
(12) Caliò, L.; Salado, M.; Kazim, S.; Ahmad, S. A Generic Route of Hydrophobic Doping in Hole Transporting Material to Increase Longevity of Perovskite Solar Cells. *Joule* **2018**, *2*, 1800−1815.
(13) Ren, G.; Han, W.; Deng, Y.; Wu, W.; Li, Z.; Guo, J.; Bao, H.; Liu, C.; Guo, W. Strategies of Modifying Spiro-OMeTAD Materials for Perovskite Solar Cells: A Review. *J. Mater. Chem. A* **2021**, *9*, 4589−4625.
(14) Yin, X.; Song, Z.; Li, Z.; Tang, W. Toward Ideal Hole Transport Materials: A Review on Recent Progress in Dopant-Free Hole Transport Materials for Fabricating Efficient and Stable Perovskite Solar Cells. *Energy Environ. Sci.* **2020**, *13*, 4057−4086.
(15) Kim, S. W.; Kim, G.; Moon, C. S.; Yang, T. Y.; Seo, J. Metal-Free Phthalocyanine as a Hole Transporting Material and a Surface Passivator for Efficient and Stable Perovskite Solar Cells. *Small Methods* **2021**, *5*, No. 2001248.
(16) Yu, Z.; Wang, L.; Mu, X.; Chen, C.; Wu, Y.; Cao, J.; Tang, Y. Intramolecular Electric Field Construction in Metal Phthalocyanine as Dopant-Free Hole Transporting Material for Stable Perovskite Solar Cells with >21% Efficiency. *Angew. Chem., Int. Ed.* **2021**, *60*, 6294−6299.
(17) Cheng, M.; Li, Y.; Safdari, M.; Chen, C.; Liu, P.; Kloo, L.; Sun, L. Efficient Perovskite Solar Cells Based on a Solution Processable Nickel(II) Phthalocyanine and Vanadium Oxide Integrated Hole Transport Layer. *Adv. Energy Mater.* **2017**, *7*, No. 1602556.
(18) Molina, D.; Ruiz-Preciado, M. A.; Carlsen, B.; Eickemeyer, F. T.; Yang, B.; Flores-Díaz, N.; Álvaro-Martins, M. J.; Nonomura, K.; Hagfeldt, A.; Sastre-Santos, Á. Zinc Phthalocyanine Conjugated Dimers as Efficient Dopant-Free Hole Transporting Materials in Perovskite Solar Cells. *ChemPhotoChem* **2020**, *4*, 307−314.
(19) Hu, Q.; Rezaee, E.; Li, M.; Chen, Q.; Cao, Y.; Mayukh, M.; McGrath, D. V.; Xu, Z.-X. Molecular Design Strategy in Developing Titanyl Phthalocyanines as Dopant-Free Hole-Transporting Materials for Perovskite Solar Cells: Peripheral or Nonperipheral Substituents? *ACS Appl. Mater. Interfaces* **2019**, *11*, 36535−36543.
(20) Huang, P.; Hernández, A.; Kazim, S.; Ortiz, J.; Sastre-Santos, Á.; Ahmad, S. Molecularly Engineered Thienyl-Triphenylamine Substituted Zinc Phthalocyanine as Dopant Free Hole Transporting Materials in Perovskite Solar Cells. *Sustainable Energy Fuels* **2020**, *4*, 6188−6195.
(21) Fukuzumi, S.; Ohkubo, K.; Ortiz, J.; Gutiérrez, A. M.; Fernández-Lázaro, F.; Sastre-Santos, Á. Formation of a Long-Lived Charge-Separated State of a Zinc Phthalocyanine-Perylenediimide Dyad by Complexation with Magnesium Ion. *Chem. Commun.* **2005**, *30*, 3814−3816.
(22) Blas-Ferrando, V. M.; Ortiz, J.; Follana-Berná, J.; Fernández-Lázaro, F.; Campos, A.; Mas-Torrent, M.; Sastre-Santos, Á. Large-Size Star-Shaped Conjugated (Fused) Triphthalocyaninehexaazatriphenylene. *Org. Lett.* **2016**, *18*, 1466−1469.
(23) Fukuzumi, S.; Ohkubo, K.; Ortiz, J.; Gutiérrez, A. M.; Fernández-Lázaro, F.; Sastre-Santos, Á. Control of Photoinduced Electron Transfer in Zinc Phthalocyanine- Perylenediimide Dyad and Triad by the Magnesium Ion. *J. Phys. Chem. A* **2008**, *112*, 10744−10752.
(24) Leznoff, C. C.; Svirskaya, P. I.; Khouw, B.; Cerny, R. L.; Seymour, P.; Lever, A. B. P. Syntheses of Monometalated and Unsymmetrically Substituted Binuclear Phthalocyanines and a Pentanuclear Phthalocyanine by Solution and Polymer Support Methods. *J. Org. Chem.* **1991**, *56*, 82−90.
(25) Liao, M.-S.; Scheiner, S. Electronic Structure and Bonding in Metal Phthalocyanines, Metal=Fe, Co, Ni, Cu, Zn, Mg. *J. Chem. Phys.* **2001**, *114*, 9780−9791.
(26) Bhattacharya, S.; Reddy, G.; Paul, S.; Hossain, S. S.; Kumar Raavi, S. S.; Giribabu, L.; Samanta, A.; Soma, V. R. Comparative Photophysical and Femtosecond Third-Order Nonlinear Optical Properties of Novel Imidazole Substituted Metal Phthalocyanines. *Dyes Pigm.* **2021**, *184*, No. 108791.
(27) Doria, S.; Lapini, A.; Di Donato, M.; Righini, R.; Azzaroli, N.; Iagatti, A.; Caram, J. R.; Sinclair, T. S.; Cupellini, L.; Jurinovich, S.; Mennucci, B.; Zanotti, G.; Paoletti, A. M.; Pennesi, G.; Foggi, P. Understanding the Influence of Disorder on the Exciton Dynamics and Energy Transfer in Zn-Phthalocyanine H-Aggregates. *Phys. Chem. Chem. Phys.* **2018**, *20*, 22331−22341.
(28) Feng, Y.; Hu, Q.; Rezaee, E.; Li, M.; Xu, Z. X.; Lorenzoni, A.; Mercuri, F.; Muccini, M. High-Performance and Stable Perovskite Solar Cells Based on Dopant-Free Arylamine-Substituted Copper(II) Phthalocyanine Hole-Transporting Materials. *Adv. Energy Mater.* **2019**, *9*, No. 1901019.
(29) Ling, X.; Wu, J.; Xu, W.; Zhang, J. Probing the Effect of Molecular Orientation on the Intensity of Chemical Enhancement Using Graphene-Enhanced Raman Spectroscopy. *Small* **2012**, *8*, 1365−1372.
(30) Hu, L.; Wang, W.; Liu, H.; Peng, J.; Cao, H.; Shao, G.; Xia, Z.; Ma, W.; Tang, J. PbS Colloidal Quantum Dots as an Effective Hole Transporter for Planar Heterojunction Perovskite Solar Cells. *J. Mater. Chem. A* **2015**, *3*, 515−518.
(31) Zheng, X.; Wang, Y.; Hu, J.; Yang, G.; Guo, Z.; Xia, J.; Xu, Z.; Fang, G. Octamethyl-Substituted Pd(<scp>ii</Scp>) Phthalocyanine

https://doi.org/10.1021/acsaem.1c02039
ACS Appl. Energy Mater. 2021, 4, 10124−10135

with Long Carrier Lifetime as a Dopant-Free Hole Selective Material for Performance Enhancement of Perovskite Solar Cells. *J. Mater. Chem. A* **2017**, *5*, 24416−24424.
(32) Iagatti, A.; Doria, S.; Marcelli, A.; Angelini, N.; Notarantonio, S.; Paoletti, A. M.; Pennesi, G.; Rossi, G.; Zanotti, G.; Calogero, G.; Foggi, P. Photophysical Processes Occurring in a Zn-Phthalocyanine in Ethanol Solution and on TiO 2 Nanostructures. *J. Phys. Chem. C* **2015**, *119*, 20256−20264.
(33) Kakade, S.; Ghosh, R.; Palit, D. K. Excited State Dynamics of Zinc−Phthalocyanine Nanoaggregates in Strong Hydrogen Bonding Solvents. *J. Phys. Chem. C* **2012**, *116*, 15155−15166.
(34) Peumans, P.; Yakimov, A.; Forrest, S. R. Small Molecular Weight Organic Thin-Film Photodetectors and Solar Cells. *J. Appl. Phys.* **2003**, *93*, 3693−3723.
(35) Abramczyk, H.; Brozek-Płuska, B.; Kurczewski, K.; Kurczewska, M.; Szymczyk, I.; Krzyczmonik, P.; Błaszczyk, T.; Scholl, H.; Czajkowski, W. Femtosecond Transient Absorption, Raman, and Electrochemistry Studies of Tetrasulfonated Copper Phthalocyanine in Water Solutions. *J. Phys. Chem. A* **2006**, *110*, 8627−8636.
(36) Caplins, B. W.; Mullenbach, T. K.; Holmes, R. J.; Blank, D. A. Femtosecond to Nanosecond Excited State Dynamics of Vapor Deposited Copper Phthalocyanine Thin Films. *Phys. Chem. Chem. Phys.* **2016**, *18*, 11454−11459.
(37) Nikolaitchik, A. V. Crown Ether Substituted Monomeric and Cofacial Dimeric Metallophthalocyanines. 1. Photophysical Studies of the Free Base, Zinc(II), and Copper(II) Variants. *J. Phys. Chem. A* **1999**, *103*, 7587−7596.
(38) Ha-Thi, M.-H.; Shafizadeh, N.; Poisson, L.; Soep, B. An Efficient Indirect Mechanism for the Ultrafast Intersystem Crossing in Copper Porphyrins. *J. Phys. Chem. A* **2013**, *117*, 8111−8118.
(39) Kumar, P. H.; Venkatesh, Y.; Siva, D.; Ramakrishna, B.; Bangal, P. R. Ultrafast Relaxation Dynamics of 5,10,15,20- Meso- Tetrakis Pentafluorophenyl Porphyrin Studied by Fluorescence up-Conversion and Transient Absorption Spectroscopy. *J. Phys. Chem. A* **2015**, *119*, 1267−1278.
(40) Bhattacharya, S.; Biswas, C.; Raavi, S. S. K.; Venkata Suman Krishna, J.; Koteshwar, D.; Giribabu, L.; Venugopal Rao, S. Optoelectronic, Femtosecond Nonlinear Optical Properties and Excited State Dynamics of a Triphenyl Imidazole Induced Phthalocyanine Derivative. *RSC Adv.* **2019**, *9*, 36726−36741.
(41) Kroeze, J. E.; Savenije, T. J.; Candeias, L. P.; Warman, J. M.; Siebbeles, L. D. A. Triplet Exciton Diffusion and Delayed Interfacial Charge Separation in a Tio2/PdTPPC Bilayer: Monte Carlo Simulations. *Sol. Energy Mater. Sol. Cells* **2005**, *85*, 189−203.
(42) Abkowitz, M.; Chen, I.; Sharp, J. H. Electron Spin Resonance of the Organic Semiconductor, α -Copper Phthalocyanine. *J. Chem. Phys.* **1968**, *48*, 4561−4567.
(43) Guzy, C. M.; Raynor, J. B.; Symons, M. C. R. Electron Spin Resonance Spectrum of Copper-63 Phthalocyanin. A Reassessment of the Bonding Parameters. *J. Chem. Soc., A* **1969**, 2299−2303.
(44) Finazzo, C.; Calle, C.; Stoll, S.; Van Doorslaer, S.; Schweiger, A. Matrix Effects on Copper(Ii)Phthalocyanine Complexes. A Combined Continuous Wave and Pulse EPR and DFT Study. *Phys. Chem. Chem. Phys.* **2006**, *8*, 1942−1953.
(45) Moons, H.; Łapok, Ł.; Loas, A.; Van Doorslaer, S.; Gorun, S. M. Synthesis, X-Ray Structure, Magnetic Resonance, and DFT Analysis of a Soluble Copper(II) Phthalocyanine Lacking C−H Bonds. *Inorg. Chem.* **2010**, *49*, 8779−8789.
(46) Greiner, S. P.; Rowlands, D. L.; Kreilick, R. W. EPR and ENDOR Study of Selected Porphyrin- and Phthalocyanine-Copper Complexes. *J. Phys. Chem. A* **1992**, *96*, 9132−9139.
(47) Hathaway, B. J.; Billing, D. E. The Electronic Properties and Stereochemistry of Mono-Nuclear Complexes of the Copper(II) Ion. *Coord. Chem. Rev.* **1970**, *5*, 143−207.
(48) Hudson, A.; Luckhurst, G. R. Electron Resonance Line Shapes of Radicals in Solution. *Chem. Rev.* **1969**, *69*, 191−225.
(49) de Quilettes, D. W.; Vorpahl, S. M.; Stranks, S. D.; Nagaoka, H.; Eperon, G. E.; Ziffer, M. E.; Snaith, H. J.; Ginger, D. S. Impact of Microstructure on Local Carrier Lifetime in Perovskite Solar Cells. *Sci.* **2015**, *348*, 683−686.
(50) Kyaw, A. K. K.; Wang, D. H.; Gupta, V.; Leong, W. L.; Ke, L.; Bazan, G. C.; Heeger, A. J. Intensity Dependence of Current−Voltage Characteristics and Recombination in High-Efficiency Solution-Processed Small-Molecule Solar Cells. *ACS Nano* **2013**, *7*, 4569−4577.
(51) Shi, J.; Dong, J.; Lv, S.; Xu, Y.; Zhu, L.; Xiao, J.; Xu, X.; Wu, H.; Li, D.; Luo, Y.; Meng, Q. Hole-Conductor-Free Perovskite Organic Lead Iodide Heterojunction Thin-Film Solar Cells: High Efficiency and Junction Property. *Appl. Phys. Lett.* **2014**, *104*, No. 063901.
(52) Huang, P.; Manju; Kazim, S.; Sivakumar, G.; Salado, M.; Misra, R.; Ahmad, S. Pyridine Bridging Diphenylamine-Carbazole with Linking Topology as Rational Hole Transporter for Perovskite Solar Cells Fabrication. *ACS Appl. Mater. Interfaces* **2020**, *12*, 22881−22890.
(53) Jena, A. K.; Ikegami, M.; Miyasaka, T. Severe Morphological Deformation of Spiro-OMeTAD in (CH3NH3)PbI3 Solar Cells at High Temperature. *ACS Energy Lett.* **2017**, *2*, 1760−1761.
(54) Sanchez, R. S.; Mas-Marza, E. Light-Induced Effects on Spiro-OMeTAD Films and Hybrid Lead Halide Perovskite Solar Cells. *Sol. Energy Mater. Sol. Cells* **2016**, *158*, 189−194.

https://doi.org/10.1021/acsaem.1c02039
ACS Appl. Energy Mater. 2021, 4, 10124−10135